RESEARCH ARTICLE

INTERNATIONAL RESEARCH JOURNAL OF MULTIDISCIPLINARY TECHNOVATION

Asian Research Association

DOI: 10.54392/irjmt25217

Yttrium Doped MoO_3 Nanoplates as Photocatalysts for Enhanced Removal of Organic dyes in Aqueous Solutions

T. Usha Devi [a], D. Senthil Kumar [b], M. Gowtham [a], Senthil Kumar Nagarajan [a, *]

[a] Postgraduate and Research Department of Physics, Nanotechnology Lab, Kongunadu Arts and Science College, Coimbatore, 641029, Tamil Nadu, India

[b] Department of Physics, Vel Tech Rangarajan Dr. Sagunthala R&D Institute of Science and Technology, Chennai, Tamil Nadu, 600062, India

* Corresponding Author Email: kumarsrkvphy@gmail.com

DOI: https://doi.org/10.54392/irjmt25217

Received: 12-10-2024; Revised: 24-02-2025; Accepted: 17-03-2025; Published: 30-03-2025

Abstract: The release of organic dyes into the environment is a significant concern, as they are toxic and carcinogenic, and contribute to water pollution, posing health risks to all living beings. Effective and environmentally friendly approaches such as photocatalysts are essential to deal with organic dyes in industrial wastes. The affordable and environmentally friendly properties of MoO_3 make it a superior photocatalyst compared to other materials. In this study, explores a co-precipitation method was used to synthesize undoped and Yttrium-Doped MoO_3 nanoparticles and its analyzed using various characterization techniques. From structural analysis revealed that all the studied samples were exhibited a monoclinic structure. SEM images showed uniform nanoplate like morphology with reduced particle agglomeration at optimal doping levels which indicates that Yttrium doping concentration affects the morphology. The performance of Yttrium doping on MoO_3 nanoparticles as efficient photocatalyst was further demonstrated in the degradation of various pollutants such as MB, CV and Rh B under visible light irradiation and it shows well photocatalytic activity during the degradation of Rh B under visible light. It was found that an appropriate amount of Y^{3+} dopant can greatly increase photocatalytic activity and the sample with 7 wt. % of Y^{3+} doping exhibits the highest photocatalytic efficiency at 91.5% for Rhodamine B after 140 min of exposure to visible light. Based on kinetic analyses, the photocatalytic performance of the 7 wt.% Y^{3+} doping MoO_3 sample showed four times higher efficient than that of the undoped MoO_3. The results highlight how controlled Y^{3+} incorporation can dramatically improve the photocatalytic properties of MoO_3, positioning 7 wt.% Y^{3+}: MoO_3 as a highly promising material for environmental remediation applications.

Keywords: Yttrium Doped Moo_3, Photocatalysis, Methylene Blue, Rhodamine B, Crystal Violet, UV-Visible Light

1. Introduction

Advanced oxidation processes (AOPs), particularly those based on photocatalytic green technologies, have emerged as promising alternatives to conventional wastewater treatment methods due to their remarkable effectiveness in degrading toxic dyes [1, 2]. Among these, semiconductor photocatalysts have attracted considerable attention for their efficiency in eliminating hazardous dye pollutants [3]. Extensive examine has been devoted to understanding and optimizing photocatalytic reactions, where light energy triggers chemical transformations that break down complex dye molecules into simpler, less harmful compounds.

Photodegradation-a key mechanism in photocatalytic processes-involves the decomposition of dye molecules under the influence of sunlight or ultraviolet (UV) light. Upon exposure to light, the molecules absorb energy, undergo excitation, and subsequently alter their chemical structure through oxidation or reduction reactions. The efficiency of this process hinges on several factors intrinsic to the photocatalyst, such as a high surface area, a wide energy band gap, and the efficient generation of electron-hole pairs. A larger surface area allows more dye molecules to adsorb onto the catalyst, thereby enhancing photodegradation activity.

Numerous semiconductors have been investigated for their photocatalytic potential, including WO_3, ZnO, In_2O_3, and SnO_2, particularly when modified with dopants to improve performance [4-7]. Among them, molybdenum trioxide (MoO_3) has emerged as a promising n-type semiconductor due to its wide band gap (2.8–3.6 eV), high photoactivity, and responsiveness to both UV and visible light [8]. Its

exceptional physical and chemical properties have led to its widespread application across diverse fields such as lithium-ion batteries [9], catalysis [10], field emission [11], gas sensing [12], and optoelectronic devices including photochromic and electrochromic systems [13,14], as well as in electrode materials [15], capacitors [16], and ferromagnetic materials [17].

One strategy to further enhance the properties of MoO_3 involves the introduction of dopants, which create surface defects that can adapt and control the material's functionality. These defects not only influence the electronic band structure but can also induce spectral shifts in the UV region, thus broadening the material's photo reactivity [18]. Rare-earth (RE) dopants are known to demonstrate interesting catalytic properties, high surface basicity, and fast oxygen ion mobility which are believed to be important in photocatalytic applications [19]. Notably, the low optical phonon energy of MoO_3 compared to other metal oxides makes it particularly suitable for rare-earth (RE) doping, which can exploit its variable oxidation states [20].

Among RE elements, yttrium ions (Y^{3+}) have shown exceptional promise as dopants. Due to their 4d orbital occupancy, Y^{3+} ions introduce multiple electron configurations, which in turn modify the energy band structure, enhance the surface-to-volume ratio, and create active grain boundary centers [21]. These modifications make Y^{3+} a highly effective dopant for improving the photocatalytic behaviour of host materials like MoO_3.

In the present study, Pure and Y^{3+}-doped MoO_3 nanoparticles were synthesized with varying dopant concentrations (3, 5 and 7 wt.%) and assessed for their structural, optical, and photocatalytic properties. Specifically, the doped MoO_3 demonstrated degradation efficiencies of approximately 92% for Rhodamine B (Rh B), 64% for Methylene Blue (MB), and 30% for Crystal Violet (CV) dyes. These results confirm the potential of Y^{3+}-doped MoO_3 as a highly efficient photocatalyst for wastewater treatment applications under UV-visible irradiation.

2. Experimental Procedure

In pursuit of synthesizing high-performance photocatalysts, the study employed reagent-grade chemicals, which were further purified whenever necessary to ensure optimal reaction conditions. The preparation of both pure molybdenum trioxide (MoO_3) and yttrium-doped MoO_3 (Y^{3+}-MoO_3) was carried out using a co-precipitation method, with dopant concentrations systematically varied at 0, 3, 5, and 7 wt.%.

The synthesis of pure MoO_3 began with a stoichiometric amount (0.01 mol) of ammonium heptamolybdate tetrahydrate [$(NH_4)_6Mo_7O_{24}.4H_2O$] (AHM), dissolved in 100 mL of deionized water to form a clear solution. To initiate the reaction, concentrated hydrochloric acid (37% HCl) was gradually introduced to the solution. This mixture was then transferred to a sand bath and heated at 150 °C for two hours. During this period, the reaction progressed, leading to the formation of a colloidal suspension with a solid precipitation. After the reaction was completed, the temperature was slowly reduced to room temperature, allowing the precipitate to settle. The resultant product was then thoroughly washed and centrifuged in three cycles using distilled water and ethanol to remove residual impurities [22]. The washed precipitate was dried overnight in an oven at 80 °C. To achieve complete crystallization and remove any remaining moisture or organic residues, the dried powder underwent calcination at 450 °C in a muffle furnace for one hour. This procedure yielded phase-pure MoO_3 powder, suitable for structural and photocatalytic analysis.

For the preparation of Y^{3+} doped MoO_3 samples, a similar co-precipitation route was adopted. In this case, Solution A was prepared using the same concentration of AHM (0.01 mol) dissolved in 100 mL deionized water. Parallelly, Solution B was freshly prepared by dissolving 0.005 mol of yttrium nitrate hexahydrate $Y(NO_3)_3.5H_2O$ in another 100 mL of deionized water. The Y^{3+} doping levels 3, 5, and 7 wt.% were precisely controlled relative to the amount of MoO_3 in order to explore the influence of dopant concentration on material performance.

After mixing the solutions, the resultant powder was manually ground for 30 minutes to ensure homogeneity. The final step involved sintering the mixed powders at 450 °C using a muffle furnace through three sequential thermal cycles, promoting dopant integration and crystal development. This meticulous synthesis process enabled the formation of Y^{3+} incorporated MoO_3 nanoparticles with enhanced structural and photocatalytic properties, setting the stage for subsequent characterization and application testing.

3. Characterization

Implementation of X-ray diffractometer (Shimadzu-LabX XRD-6000, Japan) with CuKαl radiation (40 kV, 200 mA, λ = 1.540568) at 10°-80° of 2θ angle allows the identification of prepared samples' phases. NEL-SEM 4800 operates at 200 kV while analyzing the nanoparticle surface morphology and elemental components under observation at 200 kV. JEOL JEM 2100 high-resolution transmission electron microscope allows for bright and dark field imaging, lattice resolution, selective region electron diffraction at 200 kV acceleration voltage, and image recording with a Gatan orious CCD camera. Raman examinations used mini raman Microprobe Imaging system 3000 which combined with an optical microscope offering 1.5 µm resolution power and 2 cm^{-1} spectral resolution capability. Shimadzu 3600 UV–visible irradiation spectrophotometer was used to record the changes in

different dyes solutions. A photocatalytic evaluation took place for pure and MoO_3 materials containing different yttrium doping levels (0, 3, 5 and 7 wt.%).

4. Results and Discussion

4.1 X-Ray Diffraction Analysis

The XRD analysis of co-precipitation synthesized pure MoO_3 and Y^{3+} doped MoO_3 nanoparticles with concentrations from 0 to 7 wt.% appears in Figure. 1 (a). The monoclinic phase of MoO_3 nanostructure occurred through well intense diffraction peaks positioned at 2θ degrees of 23.7, 26.0, 27.6, 34.2, 39.4 and 49.0 which correspond to the crystalline planes (111), (-311), (310), (220), (-113) and (004) in pure and Y^{3+} doped MoO_3 samples. Analysis showed that the obtained peaks of monoclinic phase MoO_3 matched the reference data stored in JCPDS card number 078-1078. The analysis of pure and Y^{3+} doped MoO_3 patterns indicated that no secondary reflections existed for the 0, 3, 5 and 7 wt. % doping samples. A new reflection (*) shows up as a peak at 31.6° in the XRD pattern of the 7 wt.% Y^{3+}: MoO_3 nanoparticles is denoted in the Fig. 1(a). The substitution of Y^{3+} occurs at the sub-lattice's locations throughout the molybdenum trioxide matrix structure. $Y_2Mo_4O_{15}$ exists as a supplementary phase in this material [23]. The low intensity of diffraction from $Y_2Mo_4O_{15}$-phase reveals that it exists as an unwanted impurity substance among the main MoO_3-phase. XRD peak intensities increase when the yttrium concentration in the doping process reaches from 0 to 7 wt.%. The distinct pronounced peak proves that the synthesized materials exhibit high crystallinity quality. A high degree of crystallinity exists in the 7 wt.% doped sample when compared to its three counterparts. The XRD patterns displayed in Figure. 1 (b) show an expansion of the data between 26 and 30 degrees. The (310) peak positions of doped MoO_3 microstructures move to lower angles in comparison to pure MoO_3 structures. The increased peak shift demonstrates that dopants have been successfully integrated into the MoO_3 crystal framework without forming separate phases. Physical attributes of Y^{3+} (Y^{3+}= 1.04 Å) ions lead to PXRD peak displacement because their radius (1.04 Å) surpasses Mo^{6+} (0.56 Å). Higher radii of dopants compared to Mo will result in peak shifts to lower 2θ readings whereas smaller radii result in the opposite effect [24, 25]. The extent of shifting indicates how well dopant elements successfully integrate into the MoO_3 crystal network without forming separate phases. The analysis confirms Y^{3+} atoms efficiently replace Mo ions in MoO_3 host structure due to larger atomic radius (Y^{3+}) dopant in the MoO_3 lattice instead of Mo ions corresponding to structural distortions [26]. The crystallite size (D), calculated using Debye-Scherrer's formula [27].

$$D = \frac{k\lambda}{\beta \cos\theta} \quad (1)$$

Where, K is the Scherrer constant (0.94), λ is the wavelength of X-ray used (1.54Å), β is the full width at half maximum (FWHM) and θ is the Bragg's diffraction angle. The calculated structural parameters are showed in Table 1. Analysis indicated the crystallite size of the samples ranged from 18.31 nm to 52.90 nm and 43.29 nm and 41.17 nm in this order. The studies demonstrated that Y^{3+} dopant concentration acted as a factor which determined the crystallite dimensions. XRD spectra demonstrated that pure and Y^{3+} doped MoO_3 formed correctly and revealed the dopant density caused changes to both structural attributes and crystallite dimensions of the resulting host material.

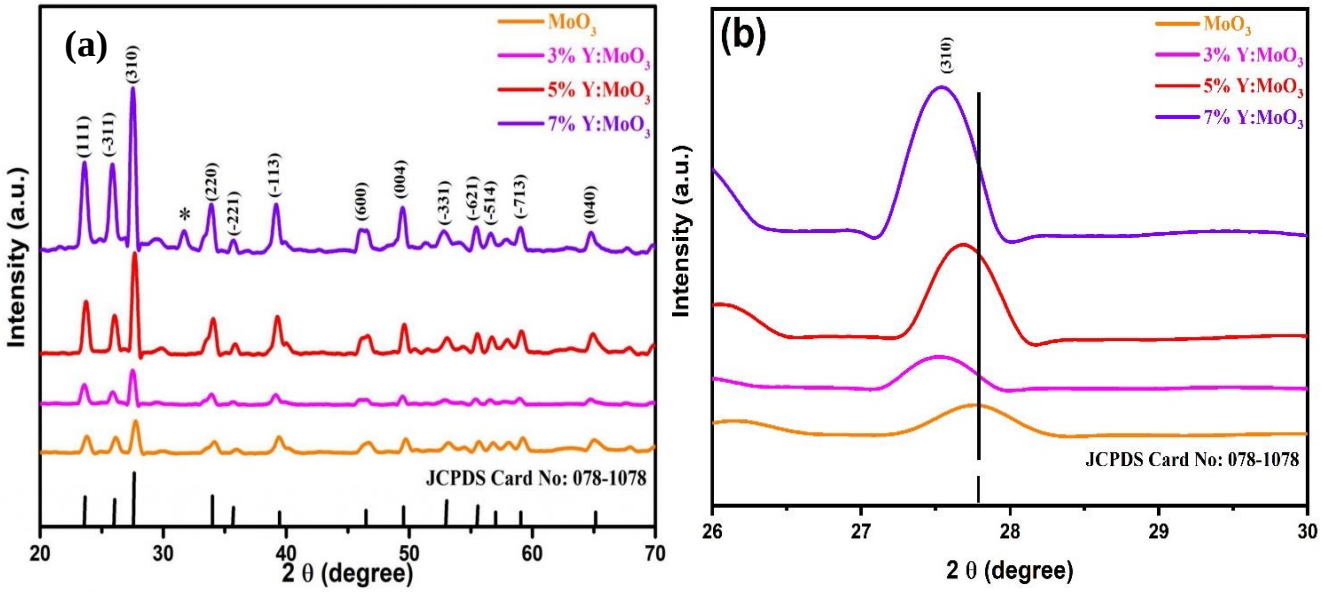

Figure1. (a) XRD analysis of pure and Y^{3+}: MoO_3 (3, 5 and 7 wt.%) nanoparticles, **(b)** Magnified image of peak (310)

Table 1. To calculated for the structural parameters of Pure and $Y3^{+}$ doped MoO_3 nanoparticles for the XRD peak (310)

Samples	FWHM (β)	Grain Size (D)
MoO_3	0.4349	18.3
Y^{3+}: MoO_3 (3%)	0.1506	52.9
Y^{3+}: MoO_3 (5%)	0.1840	43.2
Y^{3+}: MoO_3 (7%)	0.1840	41.1

4.2 FE-SEM

To gain insights into the surface morphology and structural evolution of the synthesized materials, scanning electron microscopy (SEM) was employed to analyze both pure and Y^{3+} doped MoO_3 nanoparticles at a nanometric scale. High-resolution SEM imaging at 100,000× magnification allowed detailed observation of morphological features, especially at the 100 nm scale. The SEM image of pure MoO_3, shown in Figure. 2(a), revealed a network of uniformly distributed, multiplex-shaped nanoplates measuring approximately 45 µm in length and 175 nm in width. These nanoplates were well-defined, forming a relatively consistent architecture. However, upon doping with Y^{3+} ions, subtle yet significant transformations in morphology were observed across the varying concentrations of 3, 5, and 7 wt.%.

At 3 wt.% Y^{3+} doping, as seen in Figure. 2(b), the material maintained its nanoplate-like structure, though a mild degree of agglomeration became evident. These agglomerates were randomly oriented and varied in size, suggesting that the dopant subtly disrupted the uniformity of the original structure. Notably, the Y^{3+} doped MoO_3 exhibited more consistency in shape and size compared to pure MoO_3, indicating enhanced growth control introduced by the dopant. As the concentration increased to 5 wt.%, the morphological changes became more pronounced. Figure. 2(c) highlights the emergence of a more regular substructure within the nanoplates, which displayed improved uniformity and definition. This structural refinement likely stems from the influence of Y^{3+} ions on the nucleation process, promoting a more ordered growth pattern. Interestingly, this level of doping also marked the point at which the nanocrystal size began to decrease, indicating a transition in growth dynamics.

When Y^{3+} doping reached 7 wt.%, the resulting MoO_3 structures, illustrated in Figure. 2(d), continued to exhibit the nanoplate formation but with evident changes in their dimensions. Specifically, nanorod lengths began to shrink, leading to a reduction in aspect ratio. Although the nanoplate structure was preserved, increased doping led to slight growth in overall particle size, likely due to the dopant's interference with the crystallization pathway. The observed decrease in particle dimensions throughout the samples can be attributed to the restricted nucleation and altered surface diffusion dynamics that dominate the growth mechanism.A key factor influencing these changes lies in the ionic radii mismatch between Mo^{6+} (0.65 Å) and Y^{3+} (0.90 Å). This size disparity prevents Y^{3+} from effectively substituting into the MoO_3 lattice, leading to local lattice distortions that impede crystallite growth. As a result, the introduction of Y^{3+} introduces structural disorder, altering the thermodynamic and kinetic factors governing nanoplate formation.

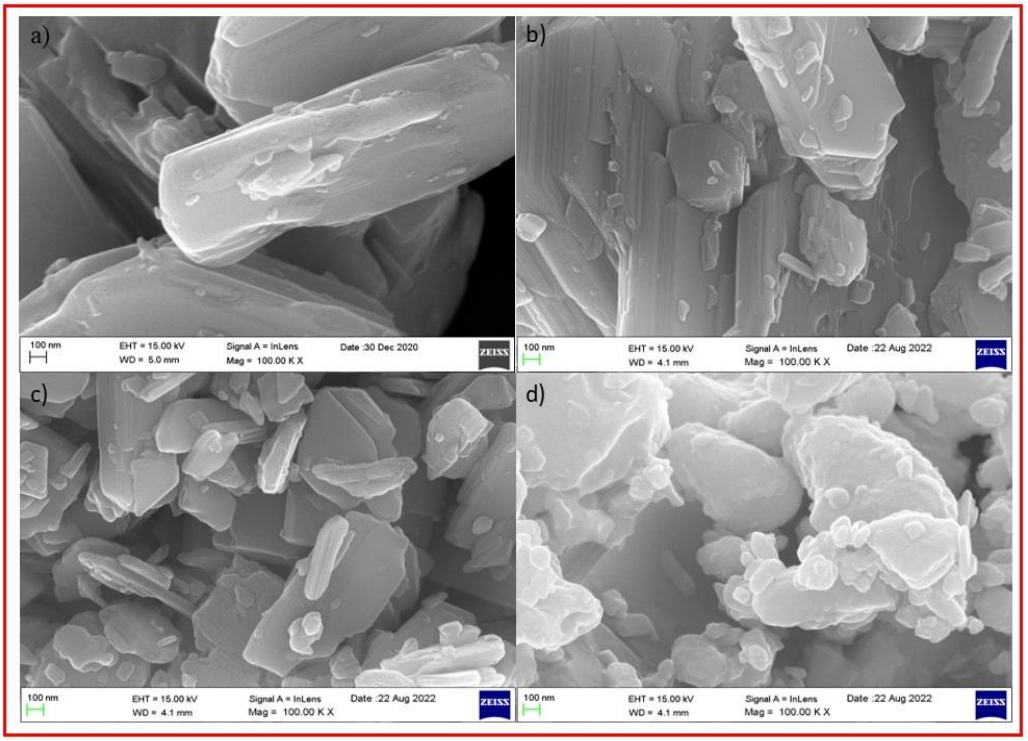

Figure 2. FESEM images of (a) Pure MoO_3 (b-d) Y^{3+}: MoO_3 (3, 5 and 7 wt.%) nanoparticles

Further SEM analysis confirmed the presence of morphology in pure MoO_3 nanoparticles (~30 nm in diameter) is sized nanoplates. This observation aligns with earlier findings by [28], who reported a similar mixed morphology in pure MoO_3 synthesized via precipitation. With Y^{3+} doping, however, the dominant morphology shifted toward finer nanoparticles with dimensions shrinking below 20 nm (Figure. 2(b–d)). The dopant appeared to function as a growth inhibitor, suppressing the natural development of large crystalline grains and promoting size reduction through lattice distortion [29].

Increased Y^{3+} content also led to a rise in bimodal particle density, with coarse-grained structures becoming more prominent. These coarser features coexisted with smaller impurities that became embedded in the voids between nanoplates, enhancing the material's packing density. The interaction between differently sized particles generated a wedging effect driven by electrostatic forces, contributing to the formation of a bimodal dispersion as supported by earlier studies [30]. Among the different concentrations examined, the 7 wt.% Y^{3+}: MoO_3 sample stood out with superior nanoplate uniformity and optimized width and length dimensions. This suggested an ideal balance between dopant-induced refinement and preservation of structural integrity, establishing it as a potentially optimal composition for further photocatalytic performance assessments.

4.3 EDAX Analysis

The Yttrium doped sample identification takes place through EDAX analysis. EDAX spectra present the compositional analysis of pure and doped samples annealed at 450°C in Figure. 3 (a–d). The acquired spectrum indicates that the sample consists of Mo, O, and Y^{3+} at trace amounts. The Table 2 provides information about elemental weight percentage and atomic percentage content according to their compositional distribution. The intensity reduction of the Mo peak indicates Y^{3+}: MoO_3 formation along with an atomic percentage decrease of oxygen. The photocatalytic properties of Y^{3+} doped MoO_3 samples develop because of the present deficiencies as shown by observation.

4.4 TEM analysis

Transmission electron microscopy (TEM) was used to analyze the structure at 200 nm and 10 nm scales, providing information about particle dimensions and morphology, as shown in Figure. 4(a–d). FESEM results appear in the TEM images which show pure MoO_3 contains nanoparticles together with few nanoplates. Most of the MoO_3 nanoplates display uniform three-dimensional structures. The pure MoO_3 nanoparticles exhibited irregular particles with sharp edges according to previous investigate [31].

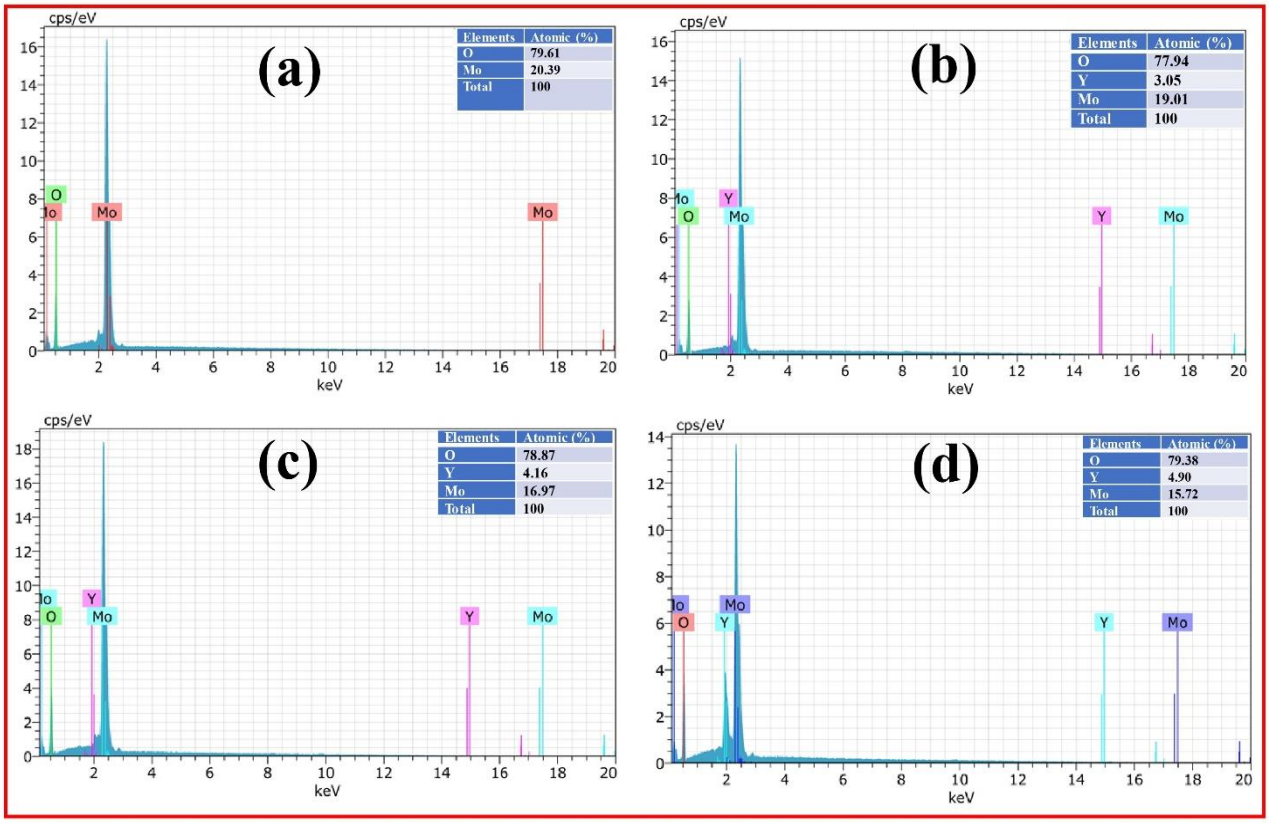

Figure 3. EDAX images of (a) pure and (b-d) Y3+: MoO3 (3, 5 and 7 wt.%) nanoparticles

Table 2. comparison the three dyes for the Maximum Degradation efficiency of Pure and Y3+: MoO3 (3, 5, 7 wt.%) nanoparticles

Samples	Degradation Efficiency (%) MB Dye	Degradation Efficiency (%) Rh B Dye	Degradation Efficiency (%) CV Dye
MoO_3	63.33	78.33	54.08
Y^{3+}: MoO_3 (3%)	46.04	91.5	66.6
Y^{3+}: MoO_3 (5%)	62.1	86.7	64.1
Y^{3+}: MoO_3 (7%)	64.0	88.4	29.5

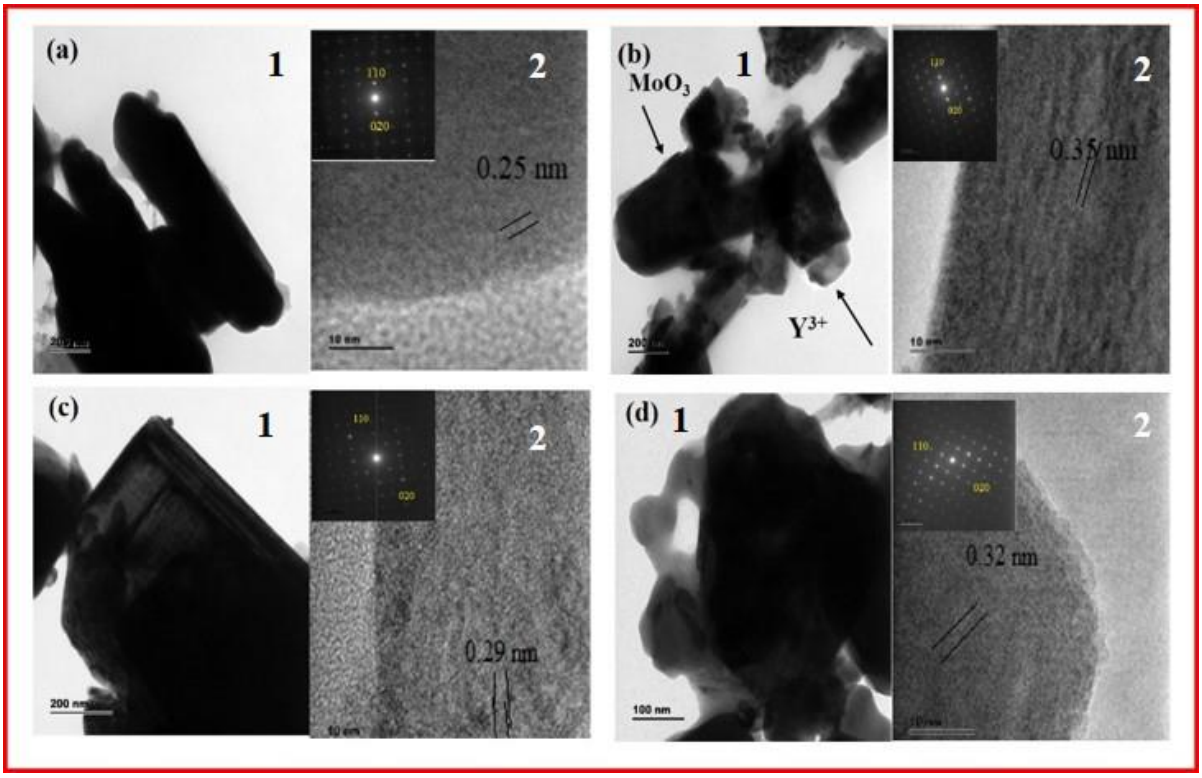

Figure 4. TEM images of **(a)** Pure MoO_3 with insert SAED Pattern and Lattice Fringes, **(b)** Y^{3+} doped MoO_3 wt. at 3% with SAED Pattern and Lattice Fringes, **(c)** Y^{3+} doped MoO_3 wt. at 5% with SAED Pattern and Lattice Fringes, **(d)** Y^{3+} doped MoO_3 wt. at 7% with SAED Pattern and Lattice Fringes

The shape evolution of synthesized MoO_3 irregular particles led to agglomerated irregular particles when yttrium ions were present during growth. The structure of MoO_3 particles became agglomerated irregular after the addition of 3 wt. % Y^{3+} doped MoO_3. Finally, varied Y^{3+} amounts led to minimal particle shape modifications. The micrographs of 3 wt. % Y^{3+} doped MoO_3 showed a severe morphological change due to the excessive growth of Y^{3+}: MoO_3 on irregular-particle MoO_3. Higher contents of Y^{3+} doped MoO_3 show clusters in TEM images while the particles exhibit reduction in their dimensions. FESEM and XRD results confirm the nanoparticle growth that Y^{3+} doping induces in the material. The recording and presentation of SAED patterns through HR-TEM images and inserted figures occurred for every analysed material. The distance between lattice planes evolves differently depending on the amount of Y^{3+} dopant according to HRTEM images. The pure MoO_3 sample showed a lattice spacing value of 0.37 nm (020) among its structure. XRD data revealed two crystals spacing of 0.37 nm (020) from pure MoO_3 together with a second spacing of 0.35 nm (111) in the 3, 5 and 7 wt.% Y^{3+} doped MoO_3 samples which signify the appearance of Y^{3+}: MoO_3 phase [32]. The TEM images confirm formation of pure and yttrium doped MoO_3 material for all doping levels including 0, 3, 5 and 7 wt.%. Each Y^{3+} increase step led to a successive material formation process.

4.5 Raman studies

Figure 5(a-d) displays the typical Raman spectra of pure MoO_3 and Y^{3+}: MoO_3 sample with three concentrations 0, 3, 5 and 7 wt. %. There are four main peaks in the 283, 665, 817 and 995 cm^{-1} frequency ranges that appear in the Raman spectra. All tested samples show Raman peaks that identify MoO_3 structure with intensity located at 817 cm^{-1}. Explore published by multiple investigations [33, 34] validates the position of these primary Raman peaks that appear in monoclinic MoO_3 crystalline phase. The bending (deformation), twisting and stretching vibrational modes of the material appear within distinct frequency ranges: between 100 and 600 cm^{-1} and between 600 and 1000 cm^{-1} respectively. The peak assignments follow the results of the single-crystal study published by Py et al [35]. The O=Mo=O wagging vibration (O=Mo=O wagging) displays its twist mode at 283 cm^{-1} while the stretching mode of triply corresponding oxygen (O–Mo–O stretch) exists at 665 cm^{-1}. The stretching mode of terminal oxygen (Mo=O stretch) manifests at 995 cm^{-1}. Within this peak range Mo=O stretch of Mo2-O (Mo=O stretch) reaches 817 cm^{-1}. As Y^{3+} concentration grows the stretching mode of vibration together with lattice mode diminishes. They indicates that band intensity grows stronger while the temperature elevation occurs. Raman scattering depends on how crystalline materials are within the spectrum because crystalline materials produce sharp intense peaks, but amorphous materials lead to less intense broader peaks. Modern studies demonstrate that the Raman spectra between crystalline and amorphous or semicrystalline solids (having identical chemical makeup) display significant variations due to differences in spatial order and long-range translational symmetry presence or absence [36]. Every peak identified in the Raman spectra belongs specifically to Pure MoO_3 nanoplates and Y^{3+} doped MoO_3 nanoparticles examined separately. The different relative peak intensities of both the lattice mode and Mo=O terminal oxygen stretching mode show evidence that structural distortion and oxygen defects occur post Y^{3+} introduction into MoO_3 nanoplates.

4.6 Photocatalytic Studies

Deposition testing of pure and Yttrium doped materials exposed three dyes to Methylene Blue (MB), Rhodamine B (Rh B) and Crystal Violet (CV). The degradation process of MB Rh B and CV dyes occurred through the observation of peaks at 665 nm, 554 nm and 590 nm. Testing for degradation efficiency of the samples occurred intermittently during twenty-minute periods. The absorption signal intensities drop in a controlled manner when the irradiation time extends.

Investigators studied the MB dye breakdown course for pure MoO_3 and Y^{3+}: MoO_3 (3, 5 and 7 wt. %) crystals when using visible light irradiation. Visible light exposure of MB dye resulted in a continuous decrease of its chemical compound amounts. The visible light irradiation duration led to distinct changes in MB dye absorbance which the Figure 6 (a) depicts. The degradation rate for MB dye through visible light radiation reached 63.33%, 46.04%, 62.1% and 64.0% based on Y^{3+}: MoO_3 nanoparticle concentrations of 0, 3, 5 and 7 wt.%. The sample containing 7 wt. % MoO_3 nanoparticles exhibits the greatest photocatalytic effect among all other Y^{3+}: MoO_3 systems tested. The MoO_3 degradation performance improves through Y^{3+} doping concentrations and porous nanoplate formation that provides increased dye absorption capacity because of their abundant surface area [44]. The presence of high oxygen-deficient properties in Y^{3+}: MoO_3 nanoparticles enabled their enhanced catalytic action.

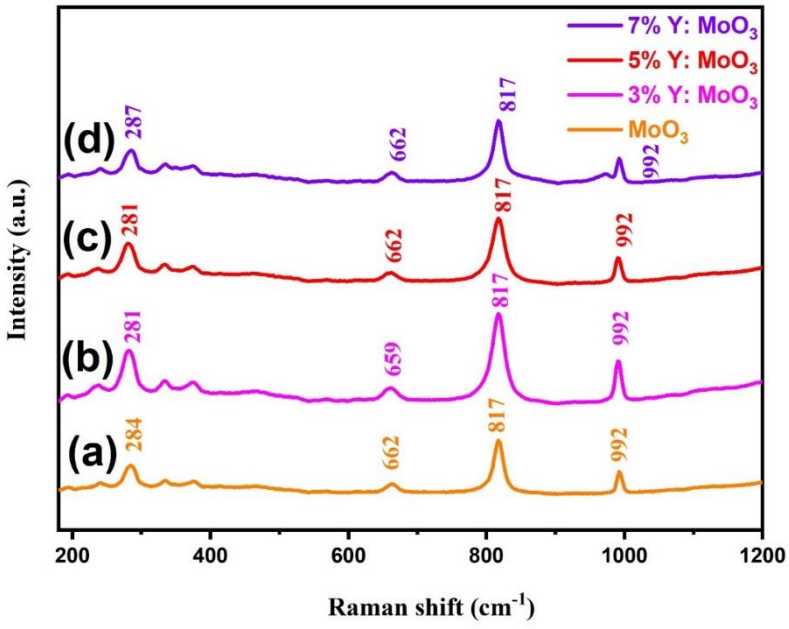

Figure 5. Raman spectrum of **(a)** pure and **(b-d)** Y3+: MoO3 (3, 5 and 7 wt.%) nanoparticles

(a)

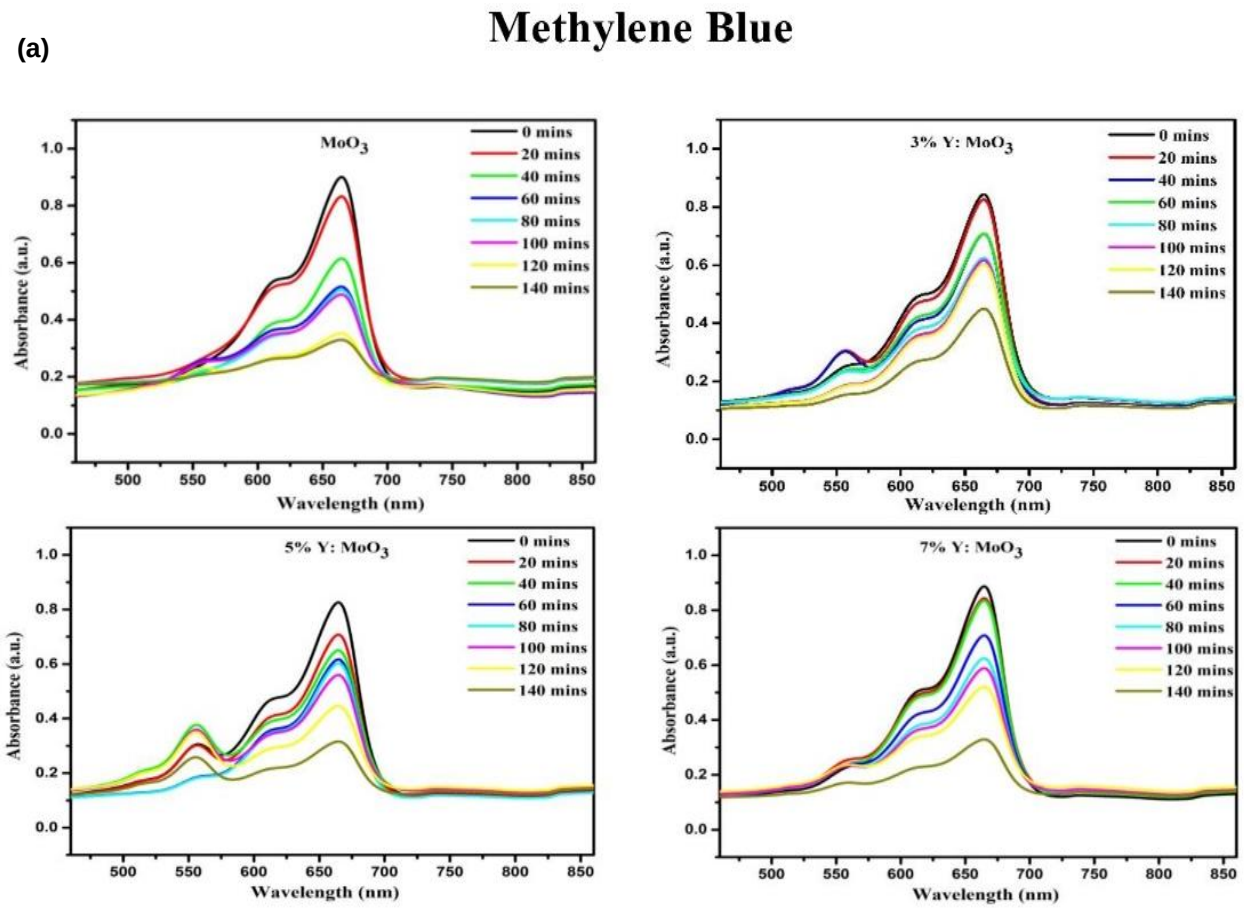

Figure 6. (a) Photocatalytic activity of Pure and Y^{3+}: MoO_3 (3, 5 and 7 wt.%) nanoparticles in Methylene Blue dye

(b)

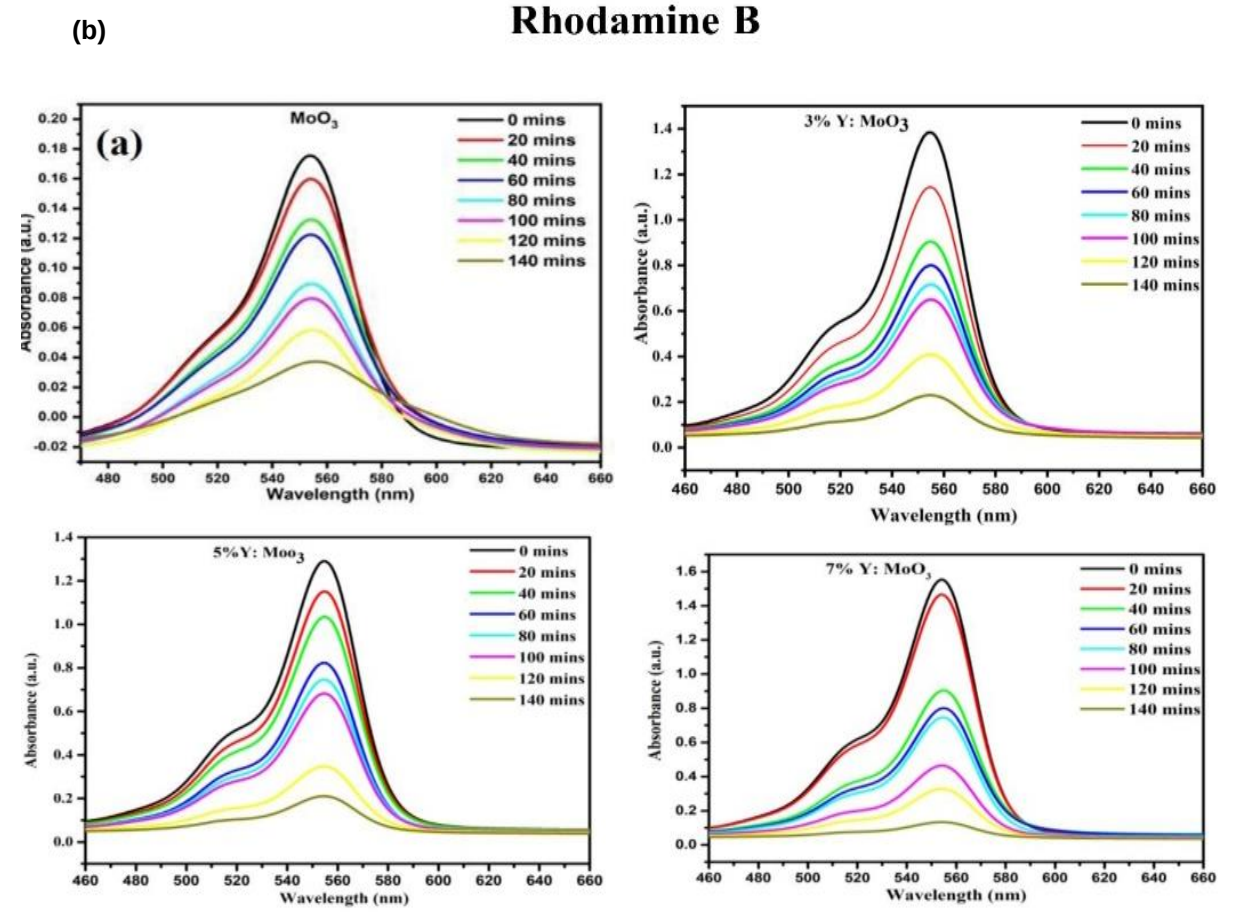

Figure 6. (b) Photocatalytic activity of Pure and Y^{3+}: MoO_3 (3, 5 and 7 wt.%) nanoparticles in Rhodamine B dye

(c)

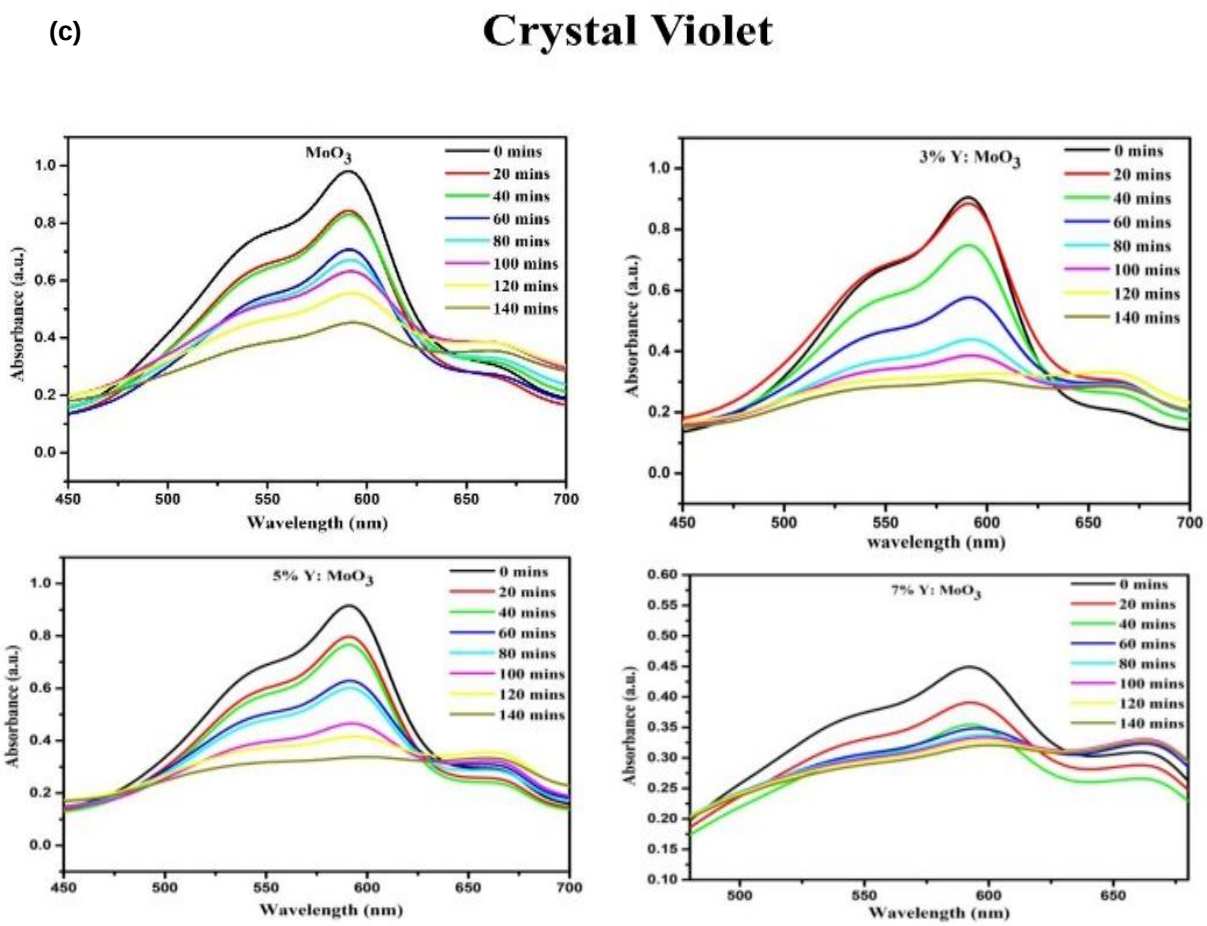

Figure 6. (c) Photocatalytic activity of Pure and Y^{3+}: MoO_3 (3, 5 and 7 wt.%) nanoparticles in Crystal Violet dye

(d)

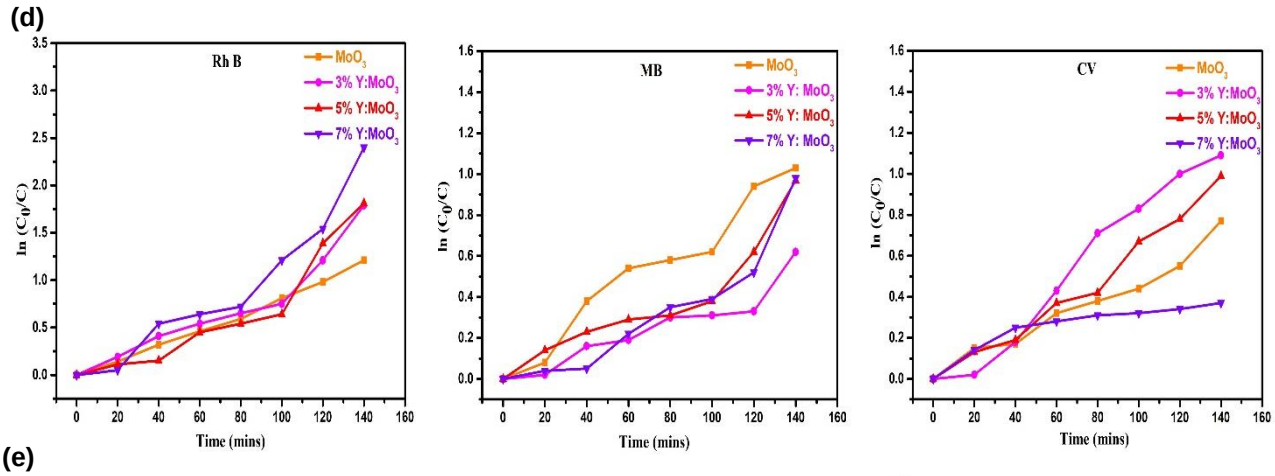

(e)

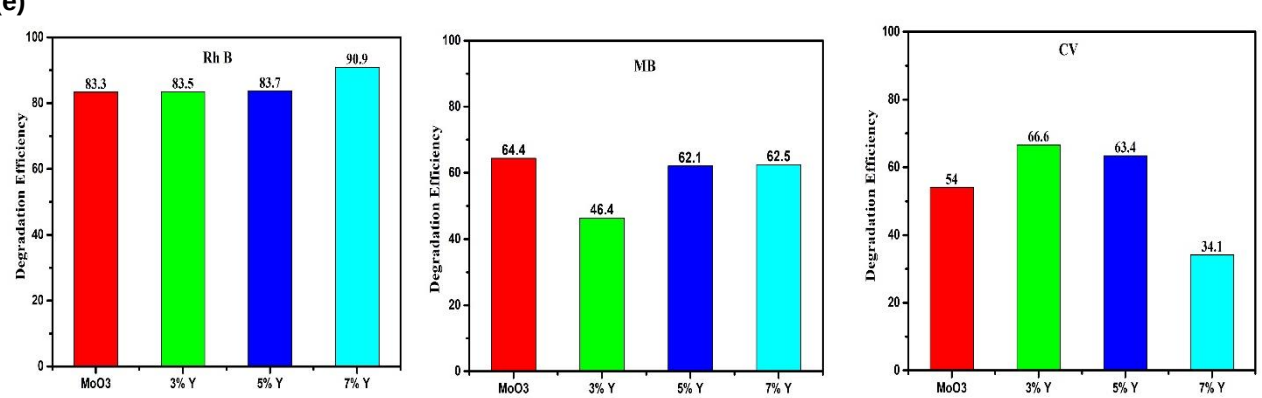

Figure 6. (d) The photocatalytic kinetics curve of pure and Y^{3+}: MoO_3 nanoparticles (e) degradation efficiency of MB, Rh B and CV dyes degradation under visible light irradiation.

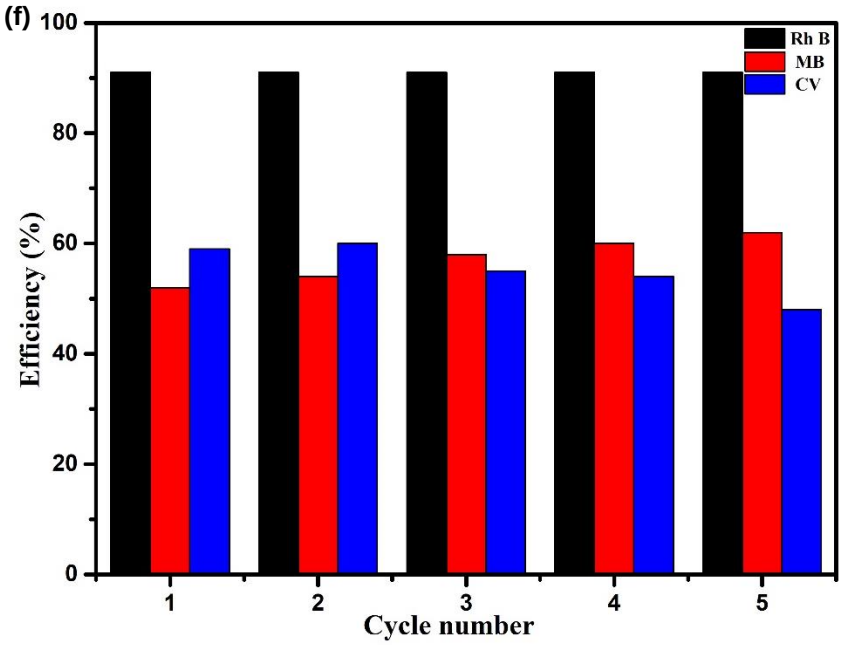

Figure 6 (f). Cycling photodegradation test of Y^{3+}: MoO_3 (7 wt. %) nanoparticles with different organic dyes

Under visible light exposure for 20 minutes the 7 wt.% Y^{3+}: MoO_3 nanoparticles achieved 50% dye color reduction that surpassed the other prepared materials which reached only 15% according to Figure 6 (b). The 7 wt.% Y^{3+}: MoO_3 sample succeeded in degrading Rh B dye by 91.5% under one hour of radiation exposure to become the most effective sample with degradation exceeding 50% for all other studied compositions. The Rh B photodegradation process reached its peak with the 7 wt.% Y^{3+}: MoO_3 sample which improved electron hole recombination while its band gap surpassed the pure and other concentration levels. The XRD and FE-SEM evaluation results indicate that materials with greater surface area enable increased molecule attachment which enhances their performance for photoactivity-related water splitting operations and catalytic reactions [38, 39].

The concentration of CV dye lowers as it interacts with visible light. The UV–vis absorption spectra show how CV dye reacts through visible light radiation at different measurement points. The degradation efficiency of CV dye reached 54% for pure MoO_3 nanoparticles but increased to 66% for Y^{3+}: MoO_3 (3 wt.%) and corresponded to 64% for Y^{3+}: MoO_3 (5 wt.%) while Y^{3+}: MoO_3 (7 wt.%) showed 29% degradation efficiency. The photocatalytic performance of Y^{3+}: MoO_3 (3 wt.%) nanoparticles surpasses all other examined samples [38]. Photoactivity became stronger in Y^{3+} doped MoO_3 because Y^{3+} served in the MoO_3 lattice structure to enable successful carrier charge separation. The increased oxygen deficiency in the Y^{3+}: MoO_3 (7% wt.%) nanoparticles contributes to better photocatalytic performance of the material.

The degradation rate constant (k) measurement of three dyes uses the pseudo-first-order kinetic model and shows up in the equation. During the degradation process the pollutant starts at a low initial concentration. The reaction rates for photocatalytic degradation appear in Fig. 6 (d). The light irradiation time against Ln (C_0/C) provides data for prepared photocatalysts in this depiction. Plots depicting color degradation percentages during degradation time can be found in the same figures. To determine the dye degradation rate following the Langmuir- Hinshelwood relationship is used Eqn. (2) [41-43].

$$Ln\,(Co/C) = kt \quad (2)$$

k represents the rate constant whereas the reaction time equals t which measures the initial dye concentration (C_0) against concentration C of three dyes. The degradation level achieved its best outcome with MoO_3 material reaching 91.5 % dye destruction rate together with rate constant 0.0406 min^{-1} while MoO_3 sample displayed minimal degradation at 78.33% along with rate constant 0.0144 min^{-1} throughout 140 minutes of light exposure. The Y^{3+}: MoO_3 (7 wt.%) nanoparticles demonstrate the best rate constant based on visible light irradiation testing making them an outstanding photocatalyst (Table 3).

The decolorization efficiency of the pure sample reaches 78% after took my measurements. At the same time, efficiency differences have decreased to values smaller than 1%. The reduction rate of Y^{3+} doped MoO_3 occurs more radically along with a faster pace. When yttrium rare-earth is added to MoO_3 the system achieves better efficiency when illuminated by ultraviolet light. The decolorization efficiency outcome relies on the quantity of utilized material. They would be incomplete without analyzing how three dyes react to visible light decolorization. The depiction of MB, Rh B and CV degradation efficiency measurements throughout irradiation duration can be observed in Figure. 6 (e).

Table 3. Stakeout the pseudo-first order rate constants (K) Pure and Y^{3+}: MoO_3 (3, 5, 7 wt.%) nanoparticles with three cationic dyes

Materials	Rate constant (K) Min $^{-1}$			Correlation coefficient (R^2)		
	Rh B	MB	CV	Rh B	MB	CV
MoO_3	**0.0144**	0.0165	0.0128	**0.8753**	1.0030	0.7781
3% Y^{3+}: MoO_3	**0.0300**	0.0102	0.0180	**1.0823**	0.6200	1.0942
5% Y^{3+}: MoO_3	**0.0306**	0.0160	0.0168	**1.8601**	0.9726	1.0249
7% Y^{3+}: MoO_3	**0.0406**	0.0168	0.0057	**2.4680**	1.0212	0.3460

The dye degradation process became faster when the Y^{3+} element was doped into MoO_3. The dye degradation using 7 wt.% Y^{3+}: MoO_3 as a photocatalyst occurred at four times the rate of MoO_3 making it suitable for possible photocatalytic usage. The removal performance achieved during the last stage of testing was equal for 7 wt. % Y^{3+}: MoO_3 but this sample showed slightly better results than others. Yttrium element addition to molybdenum trioxide particles dramatically enhances the operation speed for removal procedures. The visible light illumination promotes higher activity in all samples compared to what they achieve under UV conditions. Therefore, the longer the wavelength the better the removal efficiency. Several causational factors possibly determined the end results of degradation obtained in this process. The e^-/ h^+ recombination acts as the most significant operational challenge that reduces photocatalytic degradation performance. The principal objective of doping is to slow down charge recombination while rare-earth ions function effectively at trapping electrons so doping with these ions proves suitable for improving MoO_3's photocatalytic behavior. It demonstrates that Y^{3+} ions in MoO_3 effectively reduce recombination across the matrix structure. They identified Y^{3+} doped composites as having the most optimal general photocatalytic activity among all doping variants. The second important factor originates from the behavior of the grain microstructure. Particle size stands as a vital parameter which determines the activity in photocatalysis processes [40]. The small-sized particles during photo sensitization expand the specific surface area which facilitates degraded molecule adsorption on the catalyst surface. This is in good agreement with SEM micrographs and XRD analysis. Also, I should note that that the enhancement of the photocatalytic activity could be related to a doping-induced alteration of the MoO_3 band-gap toward higher wavelengths. Since their simultaneous effect, it is very difficult to differentiate the separate contributions of the above-mentioned factors to the overall degradation procedure, and therefore, a full analysis of results is compulsory. Figure. 6 (f) shows the photocatalytic activity efficiency for 7 wt.% Y^{3+}: MoO_3 samples over 5 cycles in the degradation of three dyes over a period of 140 minutes. Especially, ~ 91.5 % degradation of Rh B is still achieved after five cycles of photodegradation, only 7 wt.% Y^{3+}: MoO_3 sample is observed in higher efficiency when compared to other two dyes. On the other hand, 7 wt.% Y^{3+}: MoO_3 the efficiency of MB is 64 % and third dye the efficiency of 7 wt.% Y^{3+}: MoO_3 sample is around 30 %. Lower efficiency of the CV dye with 7 wt.% Y^{3+}: MoO_3 sample could be attributed to MoO_3 photocorrosion phenomenon during photocatalytic reactions [44, 45]. On the other hand, doping alkali metal elements can increase the photocorrosion resistance by increasing the chemical stability of MoO_3 during photocatalytic activity [46]. The above results demonstrated that the morphology of MoO_3 nanomaterials played an important role in the photocatalytic property, and more efforts still need to be done on how to enhance the photocatalytic activity of MoO_3 nanomaterials and clarify the photocatalytic mechanism to facilitate the application on pollutants degradation.

This paper explained the exceptional photocatalytic behavior of pure and yttrium doped MoO_3 nanoparticles with various concentrations by comparing their data with previously published studies about three dyes (Rh B, MB, CV) as well as Pure MoO_3 and yttrium doped MoO_3 nanoparticles sample degradations (Table 4 [47-60]).

Finally the photocatalytic degradation efficiencies of three dyes Methylene Blue (MB), Rhodamine B (Rh B) and Crystal Violet (CV) in pure Y^{3+}: MoO_3 (3, 5 and 7 wt.%) samples. Dye degradation reached > 91.5% for three organic substances when exposing them to visible light for 140 minutes of irradiation time. Tests indicate that Y^{3+}: MoO_3 (7 wt.%) nanoparticles hold potential for visible light degradation of Rhodamine B dye.

.

Table 4. Comparative performance of photocatalytic activity Pure and Y^{3+}: MoO_3 (3, 5, 7 wt.%) nanoparticles with different dyes

S. No	Materials	Concentration (%)	Dye	Light source	Maximum Mins	Dye degradation (%)	Ref.
1	**MoO_3**		MB	UV light	180	13	[47]
	Y: MoO_3	10				88	
2	**MoO_3**		MB	UV-Visible light	90	96	[48]
	Ni-MoO_3	15				77	
3	**MoO_3**		MB	Visible light	5 hrs	18	[49]
	Zn-MoO_3	5				43.6	
4	**MoO_3**		MB	Visible light	100	96.2	[50]
	Zn-MoO_3	15				96.8	
5	**MoO_3 -CdS**		Rh B	Visible light	180	97	[51]
6	**AgBr/MoO_3**	1:3	Rh B	Visible light	5	95	[52]
7	**MoO_{3-x}**	88 mmol	MO	Visible light	120	95.4	[53]
				NIR light		76.5	
8	**C_3N_4/MoO_3**	20% wt	Rh B	Visible light	180	93	[54]
	g-C_3N_4/MoO_3				120	71.8	
9	**MoO_3**		MB	UV-Vis Light		91	[55]
	MoO_3/$CoFe_2O_3$		Rh B			54	
	MoO_3/$CoFe_2O_3$		CV			65	
10	**CeO_2 -Y_2O_3**	pH - 9.0	Rh B	UV light	210	52	[56]
11	**MoO_{3-x} Ag/MoO_{3-x}**	65%wt	Rh B	Visible light	12	54	[57]
12	**α-MoO_3**		MB	Visible light	50	99	[58]
13	**MoO_3**		Rh B	Visible light	80	90	[59]
14	**α-MoO_3**		Rh B MB	Visible light	90	95 95	[60]
15	**MoO_3**		Rh B MB CV	UV-Visible Light	140	78.3 63.3 54.0	Present work
	Y^{3+}: MoO_3	**3%**	Rh B MB CV			88.4 46.0 66.6	
	Y^{3+}: MoO_3	**5%**	Rh B MB CV			86.7 62.1 64.1	
	Y^{3+}: MoO_3	**7%**	Rh B MB CV			91.5 64.0 29.5	

5. Conclusion

A co-precipitation process served to manufacture MoO_3 nanoplates for UV-visible light photocatalysis through the utilization of Yttrium concentration variations. The analysis through XRD patterns shows that all prepared MoO_3 along with Y^{3+}: MoO_3 samples adopt a monoclinic crystal structure Controlled observation through FE-SEM reveals that all prepared samples have nanoplate like structure. The 7 wt. % Y^{3+}: MoO_3 sample stood out with superior nanoplate uniformity and optimized width and length dimensions. The MoO_3 crystal displayed a nearly nanoplate structure according to HR-TEM measurements and it achieved its maximum average size among all emulsions within the sample containing 7 wt. % Y^{3+}: MoO_3. The Raman spectroscopic investigation verifies the stable monoclinic phase of the MoO_3 following doping since it matches XRD data. The XRD and FT-IR examination reveals how strong functional groups enter the other samples when using 7 wt. % yttrium doped MoO_3 nanoparticles. The high efficiency of Rh B dye degradation achieved 91.5% proves that 7 wt. % Y^{3+}: MoO_3 is superior to other dyes and other samples tested. 7 wt. % Y^{3+}: MoO_3 promotes the photocatalytic action of other MoO_3 powder by providing higher active sites because of its small crystals with great surface area. The photocatalytic decomposition of Rh B molecules mostly involves hole participation as the main reactive species.

References

[1] W.S.A. El-Yazeed, A.I. Ahmed, Photocatalytic activity of mesoporous WO3/TiO2 nanocomposites for the photodegradation of methylene blue. Inorganic Chemistry Communications, 105, (2019) 102-111. https://doi.org/10.1016/j.inoche.2019.04.034

[2] M. Pirhashemi, A. Habibi-Yangjeh, S. Rahim Pouran, Review on the criteria anticipated for the fabrication of highly efficient ZnO-based visible-light-driven photocatalysts. Journal of industrial and engineering chemistry, 62, (2018) 1-25. https://doi.org/10.1016/j.jiec.2018.01.012

[3] M. M.J. Sadiq, U.S. Shenoy, D.K. Bhat, Synthesis of $BaWO_4$/NRGO–gC_3N_4 nanocomposites with excellent multifunctional catalytic performance via microwave approach. Frontiers of Materials Science, 12, (2018) 247-263. https://doi.org/10.1007/s11706-018-0433-0

[4] H.M. Martínez, J. Torres, M.E. Rodríguez-García, L.L. Carreño, Gas sensing properties of nanostructured MoO_3 thin films prepared by spray pyrolysis. Physica B: Condensed Matter, 407(16), (2012) 3199-3202. https://doi.org/10.1016/j.physb.2011.12.064

[5] L. Zheng, Y. Xu, D. Jin, Y. Xie, Novel metastable hexagonal MoO3 nanobelts: synthesis, photochromic, and electrochromic properties. Chemistry of Materials, 21(23), (2009) 5681-5690. https://doi.org/10.1021/cm9023887

[6] K. Sakaushi, J. Thomas, S. Kaskel, J. Eckert, Aqueous solution process for the synthesis and assembly of nanostructured one-dimensional α-MoO_3 electrode materials. Chemistry of Materials, 25(12), (2013) 2557-2563. https://doi.org/10.1021/cm401697z

[7] A.C. Dillon, L.A. Riley, Y.S. Jung, C. Ban, D. Molina, A.H. Mahan, A.S. Cavanagh, S.M. George, S.H. Lee, HWCVD MoO_3 nanoparticles and a-Si for next generation Li-ion anodes. *Thin Solid Films*, *519*(14), (2011) 4495-4497. https://doi.org/10.1016/j.tsf.2011.01.337

[8] J. Li, X. H. Liu, Preparation and characterization of α-MoO_3 nanobelt and its application in supercapacitor. Materials Letters, 112, (2013) 39-42. https://doi.org/10.1016/j.matlet.2013.08.094

[9] Q. Qu, W.B. Zhang, K. Huang, H.M. Chen, Electronic structure, optical properties and band edges of layered MoO_3 a first principles investigation. Computational Materials Science, 130, (2017) 242–248. https://doi.org/10.1016/j.commatsci.2017.01.014

[10] A.V. Avani, E.I. Anila, Recent advances of MoO3 based materials in energy catalysis: Applications in hydrogen evolution and oxygen evolution reactions, International Journal of Hydrogen Energy, 47 (2022) 20475-20493. https://doi.org/10.1016/j.ijhydene.2022.04.252

[11] D. Jiang, W. Wei, F. Li, Y. Li, C. Liu, D. Sun, C. Feng, S. Ruan Xylene gas sensor based on α-MoO_3/α-Fe_2O_3 heterostructure with high response and low operating temperature. RSC Advances, 5, (2015) 39442–39448. https://doi.org/10.1039/C5RA05661F

[12] M. Luo, Y. Liu, J. Hu, H. Liu, J. Li (2012) One-pot synthesis of CdS and Ni-doped CdS hollow spheres with enhanced photocatalytic activity and durability. ACS applied materials & interfaces, 4(3), 1813-1821. https://doi.org/10.1021/am3000903

[13] A.A. Bernardes, C. Radtke, M.D.C.M. Alves, I.M. Baibich, M. Lucchese, J.H.Z. dos Santos, Synthesis and characterization of SiO_2–CrO_3, SiO_2–MoO_3, and SiO_2–WO_3 mixed oxides produced using the non-hydrolytic sol–gel process. Journal of sol-gel science and technology, 69, (2014) 72-84. https://doi.org/10.1007/s10971-013-3188-1

[14] L. Zhou, L. Yang, P. Yuan, J. Zou, Y. Wu, C. Yu, α-MoO_3 nanobelts: a high performance cathode material for lithium ion batteries. The Journal of Physical Chemistry C, 114(49), (2010) 21868-21872. https://doi.org/10.1021/jp108778v

[15] A. Manivel, G.J. Lee, C.Y. Chen, J.H. Chen, S.H. Ma, T.L. Horng, J.J. Wu, Synthesis of MoO_3

nanoparticles for azo dye degradation by catalytic ozonation. Materials Research Bulletin, 62, (2015) 184-191. https://doi.org/10.1016/j.materresbull.2014.11.016

[16] Z. Chen, D. Cummins, B.N. Reinecke, E. Clark, M.K. Sunkara, T.F. Jaramillo, Core–shell MoO_3–MoS2 nanowires for hydrogen evolution: a functional design for electrocatalytic materials. Nano letters, 11(10), (2011) 4168-4175. https://doi.org/10.1021/nl2020476

[17] Y.B. Li, Y. Bando, D. Golberg, K. Kurashima, Field emission from MoO_3 nanobelts. Applied Physics Letters, 81(26), (2002) 5048-5050. https://doi.org/10.1063/1.1532104

[18] A.K. Prasad, D.J. Kubinski, P.I. Gouma, Comparison of sol–gel and ion beam deposited MoO_3 thin film gas sensors for selective ammonia detection. Sensors and Actuators B: Chemical, 93, (2003) 25–30. https://doi.org/10.1016/S0925-4005(03)00336-8

[19] B. Zhao, J. Wang, H. Li, H. Wang, X. Jia, P. Su, The influence of yttrium dopant on the properties of anatase nanoparticles and the performance of dye-sensitized solar cells. Physical Chemistry Chemical Physics, 17(22), (2015) 14836-14842. https://doi.org/10.1039/C5CP01178G

[20] M. Vila, C. Díaz-Guerra, K. Lorenz, J. Piqueras, I. Píš, E. Magnano, C. Munuera, E. Alves, M.García-Hernández, Effects of thermal annealing on the structural and electronic properties of rare earth-implanted MoO_3 nanoplates. Crystal Engineering Communications, 19(17), (2017) 2339-2348. https://doi.org/10.1039/C7CE00242D

[21] C. Li, M. Liu, Y. Zeng, D. Yu, Preparation and properties of yttrium-modified lead zirconate titanate ferroelectric thin films. Sensors and Actuators A: Physical, 58(3), (1997) 245-247. https://doi.org/10.1016/S0924-4247(97)01400-3

[22] A.L. Al-Alotaibi, N. Altamimi, E. Howsawi, K.A. Elsayed, I. Massoudi, A.E. Ramadan, Synthesis and Characterization of MoO_3 for Photocatalytic Applications. Journal of Inorganic and Organometallic Polymers and Materials, 31, (2021) 2017-2029. https://doi.org/10.1007/s10904-021-01939-w

[23] G. Yan, W. Zhang, Y. Huang, P. Zhang, J. Li, Luminescence enhancement for Y_2 Mo_4O_{15}: Pr^{3+} red-emitting phosphors by Tb^{3+} co-doping. Journal of Materials Science: Materials in Electronics, 30, (2019) 14589-14599. https://doi.org/10.1007/s10854-019-01831-x

[24] H. Qin, J. Xie, H. Xu, Y. Li, Y. Cao, Green solid-state chemical synthesis and excellent xylene-detecting behaviors of Y-doped α-MoO_3 nanoarrays. Materials Research Bulletin, 93, (2017) 256-263. https://doi.org/10.1016/j.materresbull.2017.05.018

[25] Massoudi, T. Ghrib, A.L. Al-Otaibi, K. Al-Hamadah, S. Al-Malky, M. Al-Otaibi, M. Al-Yatimi, Effect of yttrium substitution on microstructural, optical, and photocatalytic properties of ZnO nanostructures. Journal of Electronic Materials, 49, (2020) 5353-5362. https://doi.org/10.1007/s11664-020-08274-9

[26] B. Jansi Rani, G. Ravi, R. Yuvakkumar, Fuad Ameen, Saleh AlNadhari, S.I. Hong, Fabrication and electrochemical OER activity of Ag doped MoO_3 nanorods, Materials Science in Semiconductor Processing, 107, (2020) 104818. https://doi.org/10.1016/j.mssp.2019.104818

[27] Z.R. Khan, M. Zulfequar, M.S. Khan, Optical and structural properties of thermally evaporated cadmium sulphide thin films on silicon (100) wafers. Materials Science and Engineering: B, 174(1-3), (2010) 145-149. https://doi.org/10.1016/j.mseb.2010.03.006

[28] M. Arshad, S. Ehtisham-ul-Haque, M. Bilal, N. Ahmad, A. Ahmad, M. Abbas, J. Nisar, M.I. Khan, A. Nazir, A. Ghaffar, M. Iqbal, Synthesis and characterization of Zn doped WO_3 nanoparticles: photocatalytic, antifungal and antibacterial activities evaluation, Materials Research Express, 7(1), (2020) 015407. https://doi.org/10.1088/2053-1591/ab6380

[29] A. Yazdanbakhsh, A. Eslami, M. Massoudinejad, M. Avazpour, Enhanced degradation of sulfamethoxazole antibiotic from aqueous solution using Mn-WO_3/ LED photocatalytic process: kinetic, mechanism, degradation pathway and toxicity reduction. Chemical Engineering Journal, 380, (2020) 122497. https://doi.org/10.1016/j.cej.2019.122497

[30] X. Ye, Y. Li, Y. Ai, Y. Nie, Novel powder packing theory with bimodal particle size distribution-application in superalloy. Advanced Powder Technology, 29(9), (2018) 2280-2287. https://doi.org/10.1016/j.apt.2018.06.012

[31] J. Kaur, K. Anand, K. Anand, R.C. Singh, WO_3 nanolamellae/reduced graphene oxide nanocomposites for highly sensitive and selective acetone sensing. Journal of Materials Science, 53, (2018) 12894-12907. https://doi.org/10.1007/s10853-018-2558-z

[32] S.J. Liu, Y. Yuan, S.L. Zheng, J.H. Zhang, Y. Wang, (2015) Fabrication of C-doped WO_3 nanoparticle cluster arrays from PS-b-P4VP for room temperature H_2 sensing. *Dalton Transactions*, 44(25), 11360-11367. https://doi.org/10.1039/C5DT01369K

[33] J. Chen, M. Wang, X. Liao, Z. Liu, J. Zhang, L. Ding, L. Gao, Y. Li, Large-scale synthesis of single-crystal molybdenum trioxide nanobelts by hot-wire chemical vapour deposition. Journal of Alloys and Compounds, 619, (2015) 406-410. https://doi.org/10.1016/j.jallcom.2014.09.069

[34] M. Dieterle, G. Weinberg, G. Mestl, Raman spectroscopy of molybdenum oxides Part I. Structural characterization of oxygen defects in MoO_{3-x} by DR UV/VIS, Raman spectroscopy and X-ray diffraction. Physical Chemistry Chemical Physics, 4(5), (2002) 812-821. https://doi.org/10.1039/B107012F

[35] M.A. Py, P.E. Schmid, J.T. Vallin, Raman scattering and structural properties of MoO_3. Il Nuovo Cimento B, 38(2), (1977) 271–279. https://doi.org/10.1007/BF02723496

[36] D. Tuschel, "Why are the Raman spectra of crystalline and amorphous solids different. Spectroscopy, 32(3), (2017) 26–33.

[37] D. Li, J.F. Huang, L.Y. Cao, L. Jia-Yin, H.B. Ou Yang, C.Y. Yao, (2014). Microwave hydrothermal synthesis of Sr^{2+} doped ZnO crystallites with enhanced photocatalytic properties. Ceramics International, 40(2), 2647-2653. https://doi.org/10.1016/j.ceramint.2013.10.061

[38] I.P. Parkin, R. Palgrave, elf-cleaning coatings. Journal of materials chemistry, 15(17), (2005) 1689-1695. https://doi.org/10.1039/b412803f

[39] U. Cernigoj, U.L. Stangar, P. Trebse, U.O. Krasovec, S. Gross, Photocatalytically active TiO_2 thin films produced by surfactant-assisted solegel processing, Thin Solid Films, 495(1-2), (2006) 327-332. https://doi.org/10.1016/j.tsf.2005.08.240

[40] H. Narayan, H. Alemu, L. Setofolo, L. Macheli, Visible Light Photocatalysis with Rare Earth Ion-Doped TiO2 Nanocomposites. International Scholarly Research Notices, 2012(1), (2012) 841521. https://doi.org/10.5402/2012/841521

[41] F. Heshmatpour, S. Zarrin, A probe into the effect of fixing the titanium dioxide by a conductive polymer and ceramic on the photocatalytic activity for degradation of organic pollutants. Journal of Photochemistry and Photobiology A: Chemistry, 346, (2017) 431-443. https://doi.org/10.1016/j.jphotochem.2017.06.017

[42] S. Zarrin, F. Heshmatpour, Photocatalytic activity of TiO_2/Nb_2O_5/PANI and TiO_2/Nb_2O_5/RGO as new nanocomposites for degradation of organic pollutants. Journal of Hazardous Materials, 351, (2018) 147-159. https://doi.org/10.1016/j.jhazmat.2018.02.052

[43] Y. Bian, Y. Ma, Y. Shang, P. Tan, J. Pan, Self-integrated β-$Bi_2O_3/Bi_2O_{2.33}$@$Bi_2O_2CO_3$ ternary composites: Formation mechanism and visible light photocatalytic activity. Applied Surface Science, 430, (2018) 613-624. https://doi.org/10.1016/j.apsusc.2017.06.063

[44] K. Dai, G. Dawson, S. Yang, Z. Chen, L. Lu, Large scale preparing carbon nanotube/zinc oxide hybrid and its application for highly reusable photocatalyst, Chemical Engineering Journal, 191, (2012) 571-578. https://doi.org/10.1016/j.cej.2012.03.008

[45] S. Muthulingam, K.B. Bae, R. Khan, I.H. Lee, P. Uthirakumar, Improved daylight-induced photocatalytic performance and suppressed photocorrosion of N-doped ZnO decorated with carbon quantum dots, RSC Advances. 5(57), (2015) 46247-46251. https://doi.org/10.1039/C5RA07811C

[46] Ahmad, E. Ahmed, M. Ahmad, M.S. Akhtar, M.A. Basharat, W.Q. Khan, M.I. Ghauri, A. Ali, M.F. Manzoor, The investigation of hydrogen evolution using Ca doped ZnO catalysts under visible light illumination. Materials Science in Semiconductor Processing, 105, (2020) 104748. https://doi.org/10.1016/j.mssp.2019.104748

[47] A.L. Al-Otaibi, Yttrium doped single-crystalline orthorhombic molybdenum oxide micro-belts: synthesis, structural, optical and photocatalytic properties. Journal of Inorganic and Organometallic Polymers and Materials, 31(8), (2021) 3416-3429. https://doi.org/10.1007/s10904-021-01999-y

[48] N. Rajiv Chandar, S. Agilan, R. Thangarasu, N. Muthukumarasamy, J. Chandrasekaran, S. Arunachalam, S.R. Akshaya, Elucidation of efficient dual performance in photodegradation and antibacterial activity by a promising candidate Ni-doped MoO_3 nanostructure. Journal of Sol-Gel Science and Technology, 100, (2021) 451-465. https://doi.org/10.1007/s10971-020-05382-0

[49] A.L. Al-Otaibi, T. Ghrib, M. Alqahtani, M.A. Alharbi, R. Hamdi, I. Massoudi, Structural, optical and photocatalytic studies of Zn doped MoO_3 nanobelts. Chemical Physics, 525, (2019) 110410. https://doi.org/10.1016/j.chemphys.2019.110410

[50] N.R. Chandar, S. Agilan, N. Muthu Kumaraswamy, R. Thangarasu, (2019). An enhanced photocatalytic performance based on MoO_3 and zn doped MoO_3 Nano structures. Journal of Ovonic Research, 15(5), 287-299.

[51] Z. Shen, G. Chen, Y. Yu, Q. Wang, C. Zhou, L. Hao, Y. Li, L.He, R. Mu, Sonochemistry synthesis of nanocrystals embedded in a MoO 3–CdS core–shell photocatalyst with enhanced hydrogen production and photodegradation. Journal of Materials Chemistry, 22(37), (2012) 19646-19651. https://doi.org/10.1039/C2JM33432A

[52] B. Feng, Z. Wu, J. Liu, K. Zhu, Z. Li, X. Jin, Y. Hou , Q. Xi, M. Cong, P. Liu, Q. Gu, Combination of ultrafast dye-sensitized-assisted electron transfer process and novel Z-scheme system: AgBr nanoparticles interspersed MoO3 nanobelts for enhancing photocatalytic performance of RhB. Applied Catalysis B:

Environmental, 206, (2017) 242-251. https://doi.org/10.1016/j.apcatb.2017.01.029

[53] Q. Liu, Y. Wu, J. Zhang, K. Chen, C. Huang, H. Chen, X. Qiu, Plasmonic MoO_3-x nanosheets with tunable oxygen vacancies as efficient visible light responsive photocatalyst. Applied Surface Science, 490, (2019) 395-402. https://doi.org/10.1016/j.apsusc.2019.06.099

[54] S. Adhikari, D.H. Kim, Heterojunction C_3N_4/MoO_3 microcomposite for highly efficient photocatalytic oxidation of Rhodamine B. Applied Surface Science, 511, (2020) 145595. https://doi.org/10.1016/j.apsusc.2020.145595

[55] N. Tariq, R. Fatima, S. Zulfiqar, A. Rahman, M.F. Warsi, I. Shakir, Synthesis and characterization of $MoO_3/CoFe_2O_4$ nanocomposite for photocatalytic applications. Ceramics International, 46(13), (2020) 21596-21603. https://doi.org/10.1016/j.ceramint.2020.05.264

[56] C. Maria Magdalane, K. Kaviyarasu, J. Judith Vijaya, B. Siddhardha, B. Jeyaraj, Facile synthesis of heterostructured cerium oxide/yttrium oxide nanocomposite in UV light induced photocatalytic degradation and catalytic reduction: Synergistic effect of antimicrobial studies, Journal of Photochemistry & Photobiology, B: Biology, 173, (2017) 23-34. https://doi.org/10.1016/j.jphotobiol.2017.05.024

[57] Z.H. Zhao, J.B. Wang, J.B. Pan, Y.X. Tan, L. Chen, J.K. Guo, S. Shen, C.T. Au, S.F. Yin, Fabrication of $Ag_3PO_4/Ag/MoO_{3-x}$ Z-scheme system with excellent photocatalytic degradation performance under visible light irradiation, Materials Chemistry and Physics, 253, (2020) 123325. https://doi.org/10.1016/j.matchemphys.2020.123325

[58] R. Rathnasamy, V. Alagan, A facile synthesis and characterization of α-MoO_3 nanoneedles and nanoplates for visible-light photocatalytic application. Physica E: Low-dimensional Systems and Nanostructures, 102, (2018) 146-152. https://doi.org/10.1016/j.physe.2018.05.009

[59] M. Liao, L. Wu, Q. Zhang, J. Dai, W. Yao, Controlled morphology of single-crystal molybdenum trioxide nanobelts for photocatalysis. Journal of Nanoscience and Nanotechnology, 20(3), (2020) 1917-1921. https://doi.org/10.1166/jnn.2020.16959

[60] R. Rathnasamy, R. Thangamuthu, V. Alagan, Sheet-like orthorhombic MoO_3 nanostructures prepared via hydrothermal approach for visible-light-driven photocatalytic application. Research on Chemical Intermediates, 44, (2018) 1647-1660. https://doi.org/10.1007/s11164-017-3190-2

Authors Contribution Statement

T. Usha Devi: Writing – original draft, Validation, Software, Resources, Methodology, Investigation, Formal analysis, Data curation, D. Senthil Kumar: Formal analysis, Writing, Review and Editing. M. Gowtham-Formal analysis, Writing, Review and Editing. Senthil Kumar Nagarajan: Conceptualization. Validation, Resources, Methodology, Formal analysis, supervision and Writing – review & editing. All the authors read and approved the final version of the manuscript.

Funding

The authors declare that no funds, grants or any other support were received during the preparation of this manuscript.

Competing Interests

The authors declare that there are no conflicts of interest regarding the publication of this manuscript.

Data Availability

The data supporting the findings of this study can be obtained from the corresponding author upon reasonable request.

Has this article screened for similarity?

Yes

About the License